Carbon diffusion in bcc- and bct-Fe: Influence of short-range C–C pair interactions studied from first-principles calculations

Dmytro Kandaskalov, Liangzhao Huang, Johnathan Emo, Philippe Maugis

begindocument/before

Carbon diffusion in bcc- and bct-Fe: influence of short-range N–N interactions studied from first-principles calculations

Dmytro Kandaskalov,* Liangzhao Huang, Johnathan Emo, and Philippe Maugis†

Aix Marseille University, University Toulon, CNRS, IM2NP, Marseille, France

(Dated: March 16, 2022)

Identifying the mechanisms of interstitial diffusion in iron is important to understanding the low-temperature ageing of Fe-C ferritic and martensitic alloys. In spite of the low solubility of carbon in ferrite at equilibrium, carbon-rich areas are often found at segregated grain boundaries and in Cottrell atmospheres around dislocations. Carbon-rich areas also form by spinodal decomposition in martensite. In all these cases carbon atoms experience short-range interactions, susceptible to modify their migration behaviour. We performed first-principles calculations to study the influence of these C–C interactions on the migration of interstitial carbon in body-centred iron. The *ab initio* energy database is introduced in kinetic Monte Carlo simulations to compute the thermodynamic and kinetic parameters. We found that the migration energies of carbon are largely affected by the presence of a neighbouring carbon atom. We explain the evolution of these energies by the relative stability of the C–C configurations corresponding to stable and transition-state positions. The C–C pair interactions slightly modify the ferrite/martensite transition conditions and significantly change the carbon atomic migration path. The latter leads to an increase of the diffusivity up to 10 times and an important kinetic correlation at low temperature ($< 300\,\mathrm{K}$) and high carbon contents ($> 1\,\mathrm{at.\%}$).

I. INTRODUCTION

Many important phenomena involve impurity diffusion in solids [1]. Diffusion of small chemical elements (H, B, C, N and O) in metals typically occurs via an interstitial mechanism [2]. Among these elements, carbon occupies a special place in iron alloys as it is a most effective addition to ferritic, bainitic and martensitic steels. Through bulk diffusion, solute carbon often controls the kinetics of phase transitions: it has therefore a direct influence on the final microstructure of steels [3]. Due to the low solubility of carbon in body-centered structures, its diffusion

*Electronic address: dmytro.kandaskalov@im2np.fr
†Electronic address: philippe.maugis@im2np.fr

is usually not affected by the carbon–carbon interactions. However, carbon-rich regions are commonly observed in out-of-equilibrium structures such as supersaturated bainite or as-quenched martensite, with solute carbon fractions up to a few at% [4]. Carbon segregation at structural defects (grain boundaries and dislocations) can also raise the solute fraction up to ∼8 at% [5]. Lastly, low-temperature spinodal decomposition of martensite leads to carbon-rich body-centered regions ranging from 10 to 14 at% C [6–10].

By itself the phenomenon of carbon diffusion is important in many ways. Technological processes such as surface hardening by carburizing or nitriding are realized by interstitial diffusion [11]. Molecule-surface interactions, such as those in corrosion and heterogeneous catalysis, can also involve diffusion of adsorbed atoms into subsurface layers with further diffusion into the bulk of the material. The local stress field has a strong effect on the interstitial diffusion in iron, due to the induced deformation of the interstitial sites [12, 13]. Furthermore, interstitial diffusion causes phenomena such as internal friction [14], strain ageing [15], embrittlement [16] and steel erosion [17]. Finally, a better understanding of the interstitial diffusion mechanisms in iron will aid controlling phase transformations in steel and modelling microstructure formation in the material.

The classical measurement of carbon diffusion in ferrite was done in 1950 by Wert [18]. He showed that in the temperature range of 238–473 K, the data agree very well with a linear Arrhenius plot, which yields a diffusion barrier of 0.87 eV. After Wert, carbon diffusion in ferrite was measured with various methods and in different temperature ranges [19]. For the low-temperature linear Arrhenius regime, the assumed atomic mechanism involves carbon migration from an octahedral O-site to a nearest-neighbour O-site via a saddle point (S) (i.e., the tetrahedral T-site for an isolated carbon atom) [19–24]. Those measurements are however limited to very dilute alloys. Diffusion measurements in carbon-supersaturated alloys are difficult, owing to the instability of the solid solution, this is why results in the literature are only indirect [9, 25]. They nevertheless evidence a significant decrease in carbon diffusivity in martensite when the carbon content is increased. Theoretical analyses showed that C–C long-range elastic interactions are responsible for this decrease, via an increase of the migration barriers [12, 26].

In more carbon-rich regions, *short-range* C–C interactions cannot be neglected. There, migration of a C atom is expected to be affected by the presence of neighbouring C atoms. This short-range interaction is difficult to study by experimental techniques and thus theoretical studies at the atomic level are necessary. In 2003, Jiang et al. studied by density functional theory (DFT) the diffusion of C in ferrite [27]. Their results on single carbon atom migration correspond well to the experimental data in dilute alloys [18, 24]. This is also true for recent DFT [28] and embedded atom method (EAM) approaches [29]. However, those studies do not take into account the effects of short-range C–C interactions on diffusion. There are several theoretical works on C–C interactions when both atoms sit on octahedral interstitial sites (OO-configurations) [27, 30–32]. There is no similar study of transition-state OS-configurations, although they are essential to computing diffusion migration energies.

This article provides a multi-scale approach to study the influence of short-range C–C interactions on C migration in body-centered iron by combining *ab initio* calculations and kinetic Monte Carlo (KMC) simulations. We discuss the energetic properties of pair configurations with C–C distances up to 6 Å. One of the C atoms (called the *static* atom) occupies an O-site. The other C atom (the *migrating* atom) is positioned in an O-site (stable state) or a S-site (saddle-point state). We propose a shell-nomenclature to classify all the C–C configurations. The migration paths of a carbon atom in the presence of a neighbouring static atom are discussed and compared to the case of an isolated migrating atom. The obtained migration data are used to compute carbon order parameter and diffusion coefficients in concentrated alloys by KMC simulations.

II. METHODOLOGY

A. DFT computational techniques

In the present work, all calculations have been carried out using the Vienna Ab-initio Simulation Package (VASP) [33] based on the density functional theory (DFT). To resolve the self-consistent Kohn-Sham equations, the projected-augmented wave (PAW) method was employed [34]. The PAW method is a generalization of the pseudo-potential and linear augmented-plane-wave methods (within the frozen-core approximation) with the computational efficiency of pseudo-potential DFT algorithms. The atomic basis for PAW were $2s^2 2p^2$ and $4s^1 3d^7$ for C and Fe atoms respectively. The exchange-correlation functional PBE [35] was used to calculate the electronic structure within the generalized gradient approximation (GGA). All calculations are presented with spin polarization. The plane-wave energy cut-off was established at 400 eV for all studied systems. The supercells were $Fe_{128}C_n$, $0 \leq n \leq 2$. A $4 \times 4 \times 4$ Monkhorst and Pack grid [36] of k-points has been used for integration in the irreducible part of the Brillouin zone. These parameters were sufficient to converge the total energies down to 50 meV per supercell for studied systems.

All systems have been fully relaxed with respect to the atomic positions with constant parameters of the supercell. The atomic relaxations were performed with a conjugate-gradient algorithm. The computed cell parameter of iron (a_0 =2.825 Å) corresponds well to the other theoretical works [32, 37–40]. The computed magnetic moment of the Fe bulk is 2.16 μ_B/at which in a good agreement with experimental data 2.12μ_B/at [41].

To determine the migration minimum energy paths (MEPs), the nudged elastic band (NEB) method was used [42, 43]. The transition-state searches were carried out with the convergence criteria of 10^{-5} eV for total energies of ionic step iterations and 0.01 eV/Å for forces acting on the atoms. We used 3 images in these NEB analyses (1/4, 1/2 and 3/4 points on reaction coordinate). Then, all energy landscapes were fitted with polynomials of degree 6.

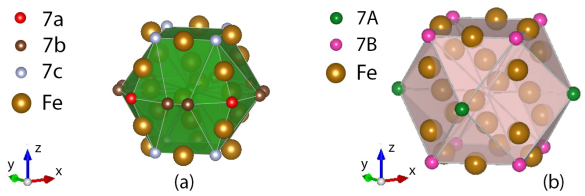

FIG. 1: The 7th shell of OT-configurations contain 20 sites distributed in 3 subshells (7a, 7b and 7c) (a) and the 7th shell of OO-configurations contain 12 sites distributed in 2 subshells (7A and 7B). In these figures, the static carbon atom is in the center of the polyhedron, in a O_z site. For OT-configurations each subshell includes the geometrically equivalent T-sites for carbon atoms: 8 sites for 7a, 4 sites for 7b and 8 sites for 7c and for OO-configurations each subshell includes the geometrically equivalent O-sites for carbon atoms: 4 sites for 7A and 8 sites for 7B

B. Stable and saddle-point configurations

To study the atomic jump of a migrating carbon atom located in the vicinity of another carbon atom, we defined two types of C–C pair configurations: an OO-configuration consists of two carbon atoms in octahedral interstitial sites, while an OT-configuration consists of one carbon atom in the octahedral site and the other in the tetrahedral site. The OO-configurations are stable and correspond to initial and final states of an elementary carbon jump. In OT-configurations, the migrating atom is located between the initial and final sites (OO-configurations). In most cases, this T site corresponds to a saddle point (S) as for single C atom migration in iron. We ranked the OO- and OT-configurations according to the distance between the carbon atoms, represented by the vector $\frac{1}{2}a_0[u,v,w]$. Notice that for a given C–C distance, several non-equivalent configurations exist. The set of all configurations sharing the same distance is referred to as a *shell* (first, second, third...). The equivalent configurations in the same shell form a *subshell*. The subshells are labelled with small letters (a, b, c...) for OT-configurations and capital letters (A, B, C...) for OO-configurations. For example, the 7th shell of OT-configuration has three subshells: 7a, 7b and 7c (see Figure 1); the 7th shell of OO-configuration has only two subshells: 7A and 7B.

In our model we studied the configurations up to the 14th shell, which represents a reasonable limit for our cubic supercell of 128 Fe atoms. The shell number N is directly related to the distance vector $\frac{1}{2}a_0[u,v,w]$: For OT-configurations the shell number is equal to

$$N_{\mathrm{OT}} = u^2 + v^2 + w^2 + \frac{3}{4}. \tag{1}$$

In the case of OO-configuration the shell number is

$$N_{\mathrm{OO}} = u^2 + v^2 + w^2 - A, \tag{2}$$

where $A = 0$ for $u^2 + v^2 + w^2 \leq 6$, $A = 1$ for $8 \leq u^2 + v^2 + w^2 \leq 15$ and $A = 2$ for $16 \leq u^2 + v^2 + w^2 \leq 23$.

The ranking of subshells is based also on the vector $\frac{1}{2}a_0[u,v,w]$. Let us take the same 7th OT-shell as an example

($N_{\mathrm{OT}} = 7$). This shell has 3 subshells defined by the vectors $\frac{1}{2}a_0[2, 1.5, 0]$, $\frac{1}{2}a_0[0, 1.5, 2]$ and $\frac{1}{2}a_0[2.5, 0, 0]$. We attribute the labels a, b and c in order of increase of $|w|$. Thus, the subshell with the vector $\frac{1}{2}a_0[0, 1.5, 2]$ is 7c. If $|w|$ is the same for several subshells, as we have in this example, we rank them by increasing the sum $|u| + |v|$. In the present case, the labels are as follows: $\frac{1}{2}a_0[2.5, 0, 0]$ is 7a and $\frac{1}{2}a_0[2, 1.5, 0]$ is 7b (see Table I).

In our work we label OT-configurations as OS-configurations taking into account that our interest consists specifically in the finding of saddle-points, however for some topological discussions when we will discuss precisely the mid position between initial and final state we will return to using OT-configurations.

We also need to introduce sublattice information for the interstitial atoms of the same shell. A carbon atom on an *octahedral* site can be of three types (O_x, O_y or O_z) depending in which sublattice (x, y or z) is located this atom. Mechanically, the presence of a carbon atom creates a prolate tetragonal distortion along the direction corresponding to its sublattice.

A carbon atom on a *tetrahedral* site creates an oblate tetragonal distortion and can be of three types (T_x, T_y or T_z) depending on direction of the oblate effect [12]. Figure 2a illustrates a carbon jump starting from an octahedral site of type z, through a tetrahedral site of type x, and ending at an octahedral site of type y, i.e. a "$z-x-y$" jump. During this path, the bcc lattice is successively tetragonally distorted along directions z, x and y. For any kind of jump, the lattice is distorted in three successive directions [28]. Each octahedral interstitial site has 4 nearest-neighbour octahedral sites. Thus any carbon atom can migrate towards 4 possible directions (Figure 2b). The 5 sites involved (central site and its 4 neighbours) are located in the same plane, which is perpendicular to the axis of the central site.

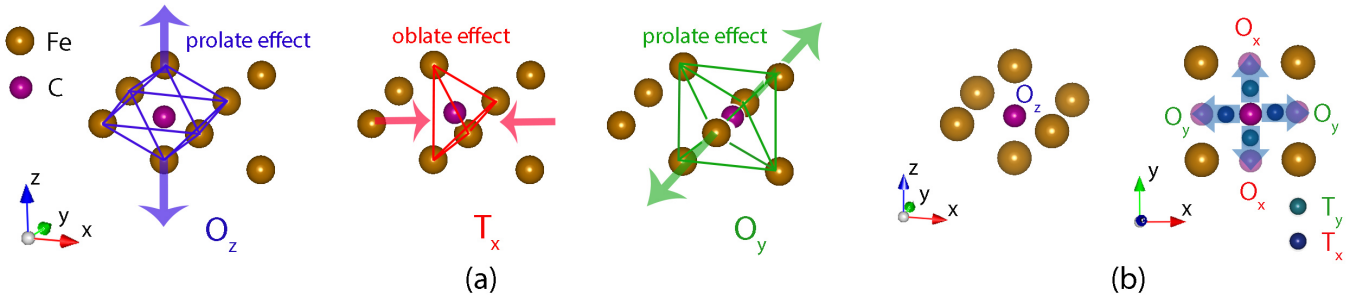

FIG. 2: (a) Tetragonal distortion effect during carbon migration from an O-site to a nearest-neighbour O-site. In the case shown, the migration path is $O_z - T_x - O_y$. (b) A carbon atom in a O_z-site has four possible jumps: two towards O_x-sites through T_y-sites, and two towards O_y-sites through T_x-sites.

Without loss of generality, the static atom was positioned on the z sublattice (O_z type of site). The migrating atom, for its part, can occupy any of the three sublattices x, y, z, which causes tetragonal distortions in one of three possible directions. Notice that these distortions do not generate additional shells because each shell is made of the same type of interstitial carbon atoms: z-type, or x- with y-type (x and y are equivalent in this respect).

C. Carbon migration barrier

For an isolated carbon atom, the migration path is symmetric since initial and final states are geometrically identical, and the saddle point is at mid-path. For this case, there is only one migration energy E_{m0}, since the direct and reverse jumps are equivalent (Figure 3a).

In the case of a pair of carbon atoms with 128 iron atoms per supercell, we used as reference energy the state of two isolated carbon atoms positioned on octahedral interstitial sites. The reference energy is therefore twice the insertion energy of carbon in O-site. The interaction energy $E_{\mathrm{C-C}}$ of a carbon–carbon pair is calculated as

$$E_{\mathrm{C-C}} = E_{\mathrm{ins}}(\mathrm{C-C}) - 2E_{\mathrm{ins}}(\mathrm{C}) \tag{3}$$

where $E_{\mathrm{ins}}(\mathrm{C})$ is the insertion energy of one carbon atom in octahedral site and $E_{\mathrm{ins}}(\mathrm{C-C})$ is the insertion energy of two neighbouring carbon atoms. $E_{\mathrm{C-C}} > 0$ means repulsion. The insertion energies are calculated as

$$\begin{aligned} E_{\mathrm{ins}}(\mathrm{C}) &= E(\mathrm{Fe_{128}C_1}) - E(\mathrm{Fe_{128}}) - E(\mathrm{C}) \\ E_{\mathrm{ins}}(\mathrm{C-C}) &= E(\mathrm{Fe_{128}C_2}) - E(\mathrm{Fe_{128}}) - 2E(\mathrm{C}) \end{aligned} \tag{4}$$

where $E(\mathrm{Fe_{128}C_2})$, $E(\mathrm{Fe_{128}C_1})$ and $E(\mathrm{Fe_{128}})$ are the energies of the $\mathrm{Fe_{128}C}_n$ systems with n =2, 1, 0 in correspondence.

In this work we are interested in three energetic parameters: C–C interaction energy $E_{\mathrm{C-C}}$ mentioned above and the direct and reverse migration energies E_{m1} and E_{m2} (Figure 3b). The direct jump is defined as the case of C–C pair dissociation (i.e. the C–C distance increases), while the reverse jump corresponds to the pair association (the C–C distance decreases).

Let us define $E_{\mathrm{C-C}}(\mathrm{OS})$ as the interaction energy in the transition state, i.e. when the migrating atom is at the saddle point. $E_{\mathrm{C-C}}(\mathrm{OO_{init}})$ and $E_{\mathrm{C-C}}(\mathrm{OO_{fin}})$ are the interaction energies at the initial and the final state respectively. Then the migration energies are simply expressed as

$$\begin{aligned} E_{\mathrm{m1}} &= E_{\mathrm{C-C}}(\mathrm{OS}) - E_{\mathrm{C-C}}(\mathrm{OO_{init}}) \\ E_{\mathrm{m2}} &= E_{\mathrm{C-C}}(\mathrm{OS}) - E_{\mathrm{C-C}}(\mathrm{OO_{fin}}) \end{aligned} \tag{5}$$

At variance to the case of an isolated carbon atom, presence of the static carbon atom breaks the symmetry of the direct and reverse jumps. Thus, as long as the interaction between the two carbon atoms exists, we expect that:

(a) The energies of the initial, transition and final states will be modified;

(b) The interaction energies $E_{\mathrm{C-C}}(\mathrm{OO_{init}})$ and $E_{\mathrm{C-C}}(\mathrm{OO_{fin}})$ will be different from zero.

In the following, we will use the energetic quantities $E_{\mathrm{C-C}}$, E_{m1} and E_{m2} to discuss the influence of the geometric parameters of various C–C pair configurations on the interaction and migration energies.

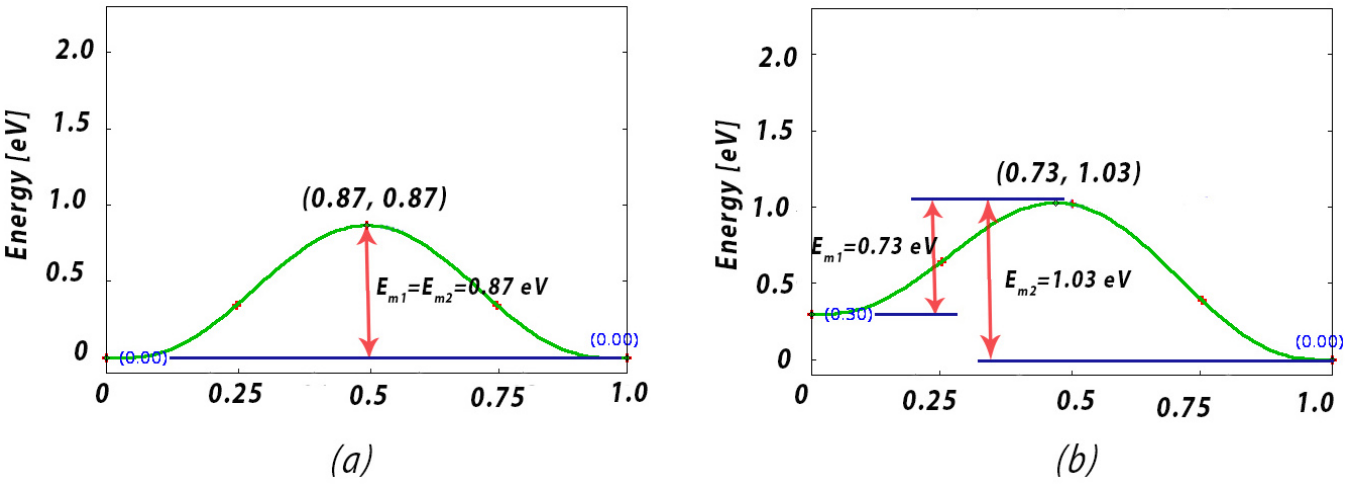

FIG. 3: (a) Migration of C atom in ferrite. The two values over the saddle point (0.87, 0.87) are right and left migration energies E_{m1} and E_{m2} (0.87 eV each). The interstitial energy of C in O-site is the energy reference. (b) An example of migration path of C atom in presence of static C atom. Here the initial and final state are different and as a consequence migration energies E_{m1} and E_{m2} are different also, the saddle point is slightly shifted from mid-path.

D. Mean-field elastic model

Zener ordering of carbon leads to a stress-strain field that affects carbon migration. Using a mean-field elastic model [9, 12], we can express the strain components as a function of the carbon content. First, we define the atom fractions $c_i = n_i/n$, where n_i is the number of carbon atoms on the octahedral sites of type $i = x$, y, z, and n is the total number of iron atoms. The total fraction $c = \sum_i c_i$ is the number of carbon atoms per iron atom in the crystal. In the case of Zener ordering along the z-direction, the order parameter is defined as $\eta = (c_z - c_{x\,\mathrm{or}\,y})/c$. In the mean-field approximation, the volume density of dipole tensor $\boldsymbol{p}$ is given by

$$\boldsymbol{p} = \frac{1}{V_0} \sum_i c_i \, \boldsymbol{P}^{O_i}, \tag{6}$$

where $\boldsymbol{P}^{O_i}$ is the dipole tensor of a carbon atom on an octahedral site of type i and V_0 is the atomic volume of iron. The carbon-induced strain tensor $\boldsymbol{\epsilon}$ at equilibrium writes

$$\boldsymbol{\epsilon} = \boldsymbol{S}\,\boldsymbol{p}, \tag{7}$$

where $\boldsymbol{S}$ is the compliance tensor of iron.

E. Kinetic Monte Carlo simulations

Kinetic Monte Carlo (KMC) simulations based on the residence-time algorithm are performed on the body-centered cubic (bcc) lattice with the octahedral sites. Periodic boundary conditions are applied to the simulation box. About

1000 carbon atoms are inserted. The size of the simulation box is adjusted by the atomic fraction of carbon atoms. They are allowed to jump during the simulation. The C-C pairwise interactions that are given by the DFT calculations are included in the carbon jump frequency:

$$\Gamma = \nu_0 \exp\left(-\frac{E_{\mathrm{m0}} + (E^{\mathrm{S}}_{\mathrm{pair}} - E^{\mathrm{O}}_{\mathrm{pair}}) - (\boldsymbol{P}^{\mathrm{S}} - \boldsymbol{P}^{\mathrm{O}}) : \boldsymbol{\epsilon}}{k_{\mathrm{B}}T}\right), \tag{8}$$

with

$$E^{\mathrm{S}}_{\mathrm{pair}} = \sum_{k\in\mathscr{S}} z_k E^k_{\mathrm{C-C}}(\mathrm{OS}),\ E^{\mathrm{O}}_{\mathrm{pair}} = \sum_{k\in\mathscr{O}} z_k E^k_{\mathrm{C-C}}(\mathrm{OO_{init}}), \tag{9}$$

where $\boldsymbol{P}^{\mathrm{S}}$ (resp. $\boldsymbol{P}^{\mathrm{O}}$) denotes dipole tensor associated to carbon atom in the saddle-point state (resp. octahedral site) and ν_0 is the attempt frequency that is assumed to be strain-independent. The values of these parameters can be found in [12]. $\mathscr{S}$ and $\mathscr{O}$ are respectively the collections of all the investigated tetrahedral and octahedral shells, and z_k is the number of carbon atoms at the k-th shell of the considered carbon atom. In order to estimate the order parameters, the occupancies of the carbon atoms are measured after each atomic jump. After the system reaches equilibrium, 100 measurements of the mean squared displacement (MSD) of the carbon atoms after 3×10^5 atomic jumps (i.e., a total of 3×10^7 carbon jumps for each simulation) are performed to compute the tracer diffusion coefficients. The relative convergence of the obtained carbon diffusivities is within $\pm 1\%$ with these settings. The tracer diffusivities D_i ($i = x$, y, z) are related to the MSD $\langle R_i^2 \rangle$ along the x, y, z directions during a period of time τ via the Einstein-Smoluchowski equation: $\langle R_i^2 \rangle = 2D_i\tau$. The MSD is given by

$$\langle R_i^2 \rangle = \left\langle \left(\sum_{n=1}^{N} R_{n,i} \right)^2 \right\rangle = f_i \left\langle \left(\sum_{n=1}^{N} R_{n,i}^2 \right) \right\rangle, \tag{10}$$

where N is the total number of jumps in the period of time τ and $R_{n,i}$ is the displacement of a carbon atom along the i-direction due to the n-th jumps. $\left\langle \left(\sum_{n=1}^{N} R_{n,i}^2 \right) \right\rangle$ is the uncorrelated MSD corresponding to the random diffusion path, and f_i is the correlation factor characterizing the deviation between the tracer diffusion and a random walk. Note that the displacements of about 1000 C atoms are simultaneously measured during the simulation. Therefore, the final MSD results from the average of all carbon atoms.

III. RESULTS AND DISCUSSION

A. Isolated carbon migration

To test our methodology, we calculated the migration energy of carbon in pure iron and compared it with experimental and theoretical literature. The experimental migration energy values are 0.86 eV [18] by Wert and 0.874 eV by Da Silva et al. [24]. These results were obtained by study of lnD evolution as 1/T function.

Theoretically, by EAM (Embedded Atom Method) calculations the migration energy of 0.81 eV was found by Garruchet et al. [44]. The DFT calculations give results in the range of 0.85 to 0.94 eV: Fors et al. 0.85 eV [45], Jiang et al. 0.87 eV [27], Souissi et al. 0.865 eV [46], Domain et al. 0.90 eV [32] and Bialon et al. 0.94 eV [47]. These results are based on NEB approaches as our or on a simple comparison of energy difference between interstitial T and O sites. Domain et al. demonstrated that smaller supercells give higher activation energies (0.92 eV for 54 atoms *vs* 0.90 eV for 128 atoms). We observe that generally theoretical results could precisely simulate experimental data by ab initio NEB approach which is more precise than EAM calculations. In the case of Domain [32] and Bialon [47] the overestimation of migration energy to the small underestimation of T-site energy stability because of symmetry imposed in their methodology.

We obtained a migration energy $E_{\mathrm{m0}} = 0.869$ eV, which agrees precisely with experimental literature and most theoretical works. Our value, obtained from volume-fixed calculations, is close to 0.875 eV calculated with cell relaxation [28]. These results allow us to conclude once more that, for 128 iron atoms per supercell, cell relaxation has a negligible effect on the migration energy.

B. OO-interactions

DFT studies of some OO-configurations have been published by Ruban [31] and by Chentouf [30] under constant supercell volume. In the present study, we recalculated a full set of OO-configurations, as they constitute input data for our NEB calculations. We also re-adapted the shell nomenclature for OO-configurations and complemented published energetic results with some extra data. In his work, Ruban computed the same configurations as ours, but the exact values for energies were given only for a few structures. We extracted approximate values out of his paper, when possible. In Chentouf's work, the precise values of energies are given, but some configurations are missing. Our energetic results correspond well to these two works [30, 31].

Our configuration nomenclature introduces shells and subshells: each *shell* corresponds to a specific distance between the carbon atoms while a *subshell* represents equivalent configurations for the same distance. In the case of OO-configurations the maximum number of subshells is two (labeled A and B), except for the 15th shell, which has 3 subshells (A, B and C).

We studied 24 configurations, which represent 14 shells plus configuration 15C (Table I and Figure 4). Most configurations have a C–C interaction energy close to zero ($|E_{\mathrm{C-C}}| < 0.05$ eV), which means that the carbon atoms can be considered as isolated. The other configurations are all repulsive. Eight configurations (1A, 2A, 3A, 4B, 7B, 8B, 10B and 14B) have energies larger than 0.15 eV, ranging from 0.16 to 2.00 eV. The most significant are presented in Figure 5. Their interaction energy is not a simple function of the bond length. For instance, configurations 4A and 4B share the same shell ($d_{\mathrm{C-C}} = a_0$), but the interaction energy in close to zero for 4A (0.01 eV) and is highly

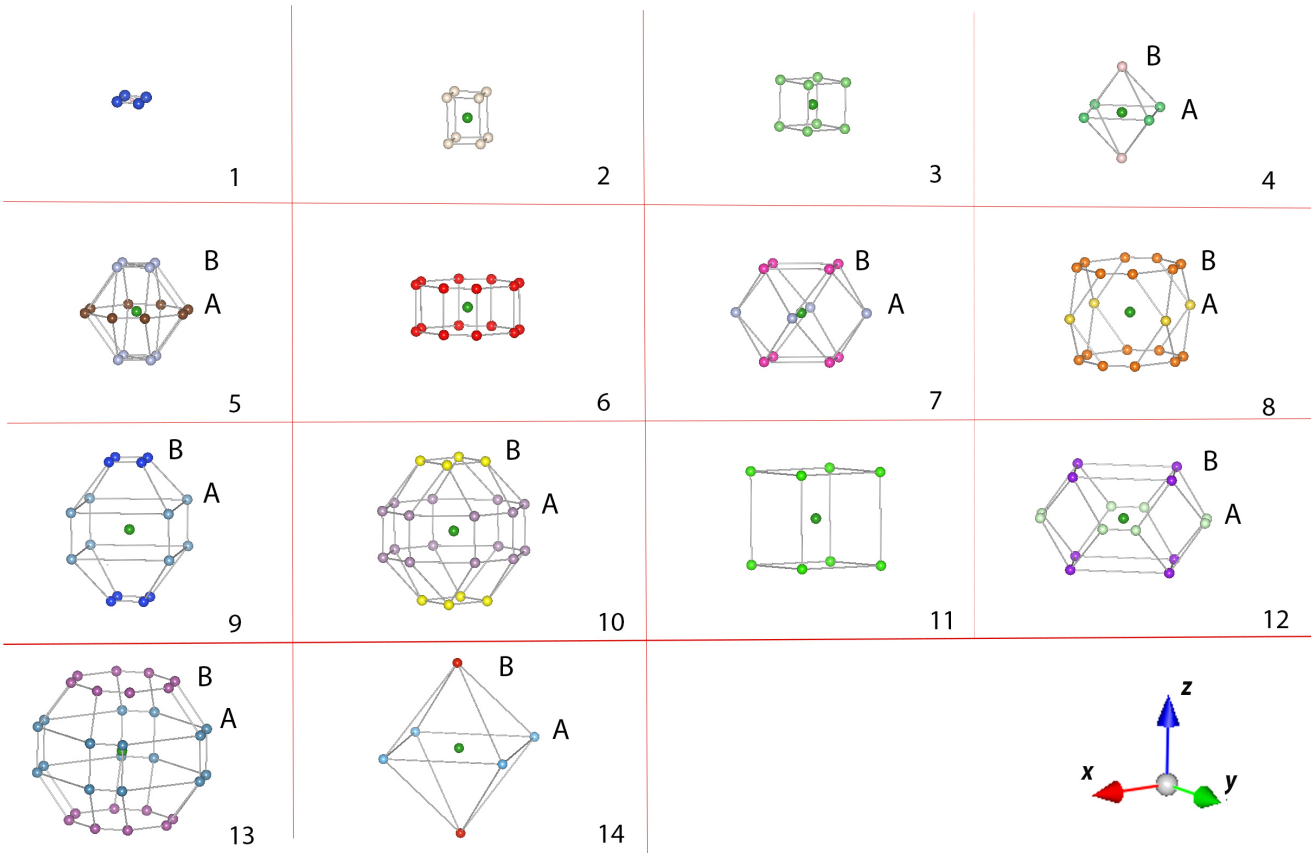

FIG. 4: The first 14 shells for OO-configurations, drawn at the same scale and the same space orientation. Different subshells inside a shell are represented by different colors and labelled in case if there is more than one subshell per shell.

repulsive for 4B (2.00 eV). This tendency is observed also for the 7th, 8th, 10th and 14th shells, where subshells A and B have quite different interaction energies, even for long bonds: e.g. 10th (4.7 Å) and 14th (5.6 Å) shells. For the cited shells, one bond is weak ($|E_{\mathrm{C-C}}| \leq 0.06$ eV) while the other is repulsive ($E_{\mathrm{C-C}} \geq 0.17$ eV). The two most repulsive configurations (1A and 4B) have interaction energies of 1.96 and 2.00 eV respectively, which corresponds to chemical repulsion. The second group of most repulsive configurations are 2A and 14B (0.83 eV). A third group of configurations (3A and 10B) has repulsive interaction energies of 0.26 and 0.30 eV.

The repulsive character of configurations 3A, 4B, 7B, 8B, 10B and 14B can be interpreted in terms of elastically interacting pairs of Fe–C–Fe dipoles. In those configurations, the two carbon atoms sit in the same O_z sublattice, such that both dipoles are parallel to the z-axis. This creates cumulative tetragonal distortions along the z-axis. Furthermore, this may shift neighbouring iron atoms in either identical or opposite directions (see Figure 6). Several cases can be distinguished. The least stable configuration 4B shows an iron atom "compressed" between 2 carbon atoms. In configuration 14B, the strong interaction corresponds to two dipoles in line. Interestingly, repulsion is not present in configuration 4A despite the proximity of the dipoles, because the shifts of neighbouring Fe atoms

are *synchronized* and the system comports similar to two isolated carbon atoms. Conversely, configuration 7B shows *antisynchronized* iron atom shifts. Compared to configuration 4A, the antisynchronized shift in configuration 7B destabilizes the structure and creates a repulsion. This is also true for configurations 3A and 10B. Notice that configuration 14B is similar to that existing in the $\alpha'' - Fe_{16}C_2$ phase (labeled 2NN' in Refs. [40, 48]).

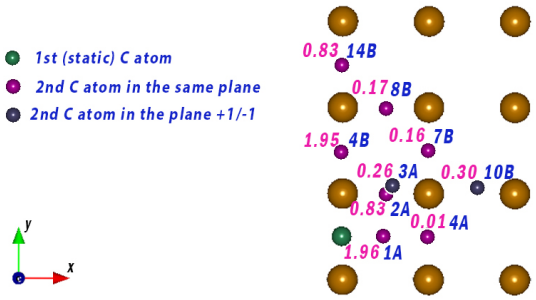

FIG. 5: Key OO-configurations illustrating the elastic dipole–dipole interaction. Static carbon atom (green), carbon atoms in the same plane (brown), carbon atoms out-of-plane in configurations 3A and 10B (violet). Each OO-configuration is labelled (in blue) and the C–C interaction energy in eV is given (in pink). The iron atoms are represented by large golden spheres.

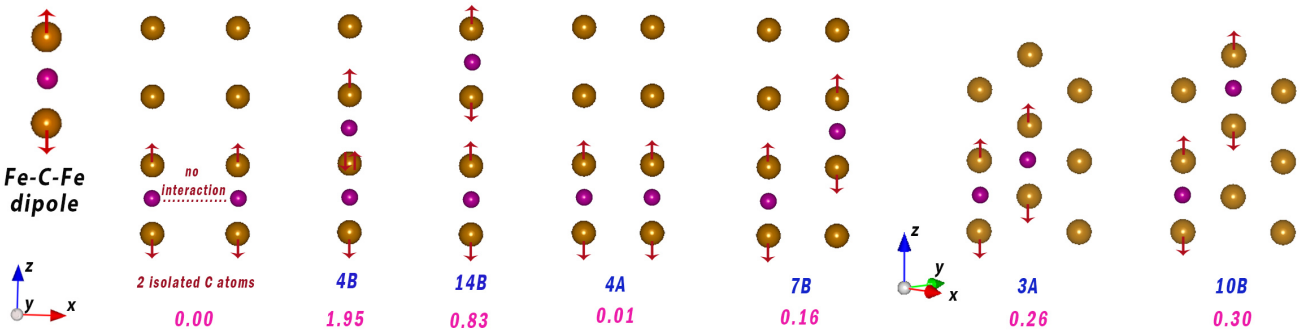

FIG. 6: Interacting pairs of Fe–C–Fe dipoles and their impact on the stability of OO-configurations. The shift of the iron atoms of a dipole along axis z is represented by a red arrow. Two dipoles exert maximum repulsion when they are in line (4B and 14B configurations). When out-of-line, two dipoles can create low-energy synchronized distortion (4A) or higher-energy antisynchronized distortion (7B and 10B). For each configuration, the label is written in blue and the interaction energy in pink.

C. OS-interactions

Using the same method, we studied the OT-configurations, which correspond to the transition states for carbon migration. The first 14 shells, corresponding to 29 configurations, are gathered in Figure 7 and Table II. The 1st shell was not considered, since its very small C–C distance ($\frac{1}{4}a_0 \simeq 0.7$ Å) is more than twice smaller than the C–C distance

TABLE I: DFT results for octahedral–octahedral carbon–carbon configurations (OO-configurations): configuration label, number of equivalent configurations (# config.), interaction energy E_{C-C} compared to literature (in eV), vector components $[u\,v\,w]$ (values in parentheses can be permuted) and bond length d_{C-C} (in a_0 units).

Configuration	# config.	E_{C-C}	ref. [30]	ref. [31]	Vectors	d_{C-C}
1A	4	1.96	1.95	2.0	[(±1 0) 0]	$\sqrt{4}/4$
2A	8	0.83	0.83	0.8	[(±1 0) ±1]	$\sqrt{8}/4$
3A	8	0.26	0.27	0.25	[±1 ±1 ±1]	$\sqrt{12}/4$
4A	4	0.01	0.02	0.0	[(±2 0) 0]	$\sqrt{16}/4$
4B	2	2.00	1.96	2.0	[0 0 ±2]	$\sqrt{16}/4$
5A	8	0.04	0.05	0.0	[(±2 ±1) 0]	$\sqrt{20}/4$
5B	8	0.04	–	0.0	[(±1 0) ±2]	$\sqrt{20}/4$
6A	16	0.07	0.07	0.0	[(±2 ±1) ±1]	$\sqrt{24}/4$
7A	4	0.03	0.03	0.0	[±2 ±2 0]	$\sqrt{32}/4$
7B	8	0.16	0.15	0.1	[(±2 0) ±2]	$\sqrt{32}/4$
8A	4	0.06	0.06	0.0	[(±3 0) 0]	$\sqrt{36}/4$
8B	16	0.17	0.17	0.1	[(±2 ±1) ±2]	$\sqrt{36}/4$
9A	8	0.07	–	0.0	[(±3 0) ±1]	$\sqrt{40}/4$
9B	8	0.07	0.07	0.0	[(±1 0) ±3]	$\sqrt{40}/4$
10A	16	0.02	0.02	0.0	[(±3 ±1) ±1]	$\sqrt{44}/4$
10B	8	0.30	0.30	0.3	[±1 ±1 ±3]	$\sqrt{44}/4$
11A	8	0.04	0.03	0.0	[±2 ±2 ±2]	$\sqrt{48}/4$
12A	8	0.00	0.00	0.0	[(±3 ±2) 0]	$\sqrt{52}/4$
12B	8	-0.01	–	0.0	[(±3 0) ±2]	$\sqrt{52}/4$
13A	16	0.00	–	0.0	[(±3 ±2) ±1]	$\sqrt{56}/4$
13B	16	0.01	0.00	0.0	[(±2 ±1) ±3]	$\sqrt{56}/4$
14A	4	-0.02	-0.02	0.0	[(±4 0) 0]	$\sqrt{64}/4$
14B	2	0.83	0.83	0.8	[0 0 ±4]	$\sqrt{64}/4$
15C	16	-0.04	–	–	[(±1 0) ±4]	$\sqrt{68}/4$

in graphite (1.42 Å) or diamond (1.54 Å). It is thus highly improbable in the bcc structure.

For OS-configurations, the shells can contain up to 5 subshells (labelled a, b, c, d and e). Since OS-configurations are not stable because one of the carbon atoms occupies a saddle point, it is not possible to obtain the C–C interaction energies for this type of configurations by a standard total energy minimization procedure. Therefore, we used the NEB method to compute the C–C interaction energy evolution during migration paths, to obtain the energies for all OS-configurations.

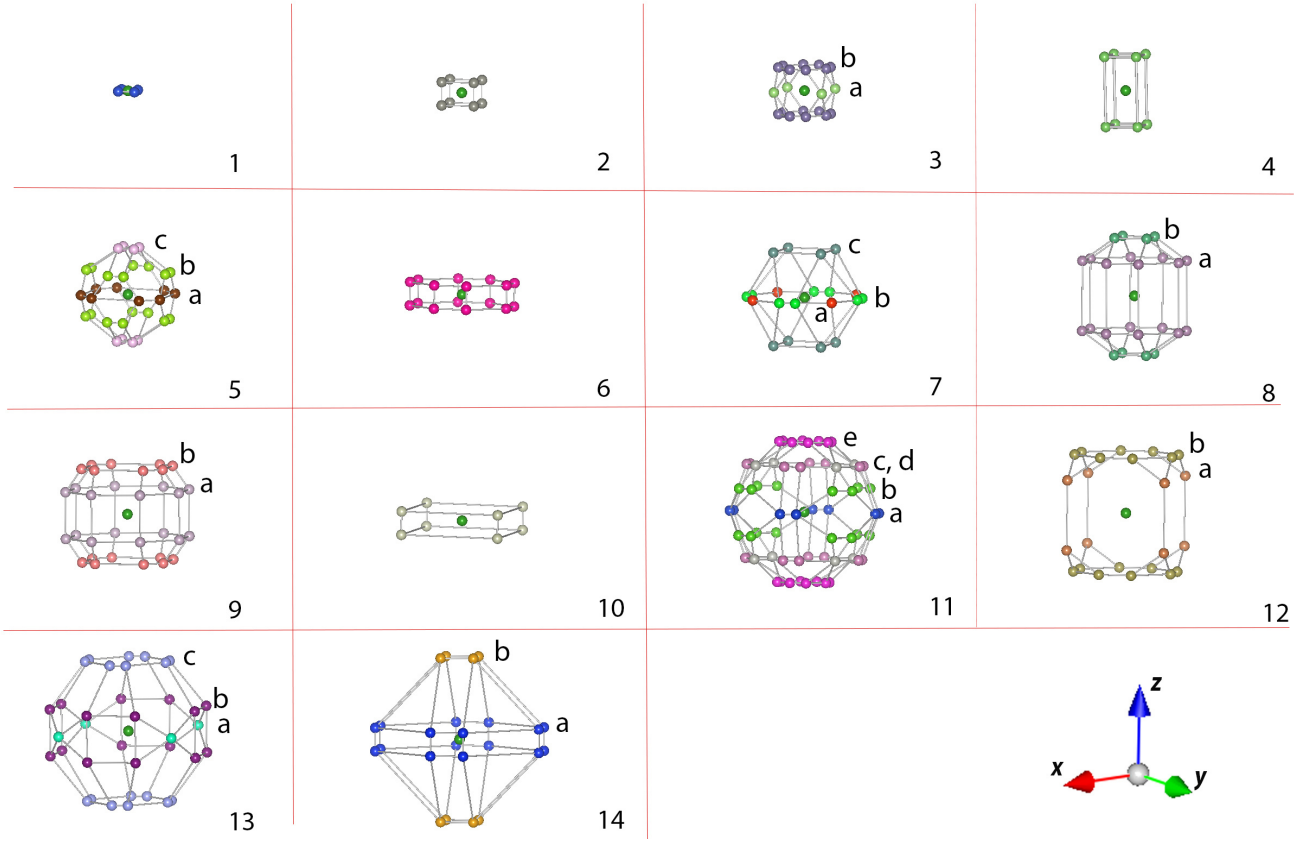

FIG. 7: The first 14 shells for OS-configurations, drawn at the same scale and the same space orientation. Different subshells inside a shell are represented by different colors and labelled in case if there is more than one subshell per shell.

We remind that for two isolated OS carbon atoms the $E_{\mathrm{C-C}}$ energy is 0.87 eV and thus if OS-interaction energy is higher than 0.87 eV it is considered as repulsive interaction (Figure 3a). The results (Table II) show us that mostly all interactions are repulsive in this way. We could see a group of interactions highly repulsive with energies from 1.38 eV up to 1.74 eV. These configurations correspond to small distances between 2 carbon atoms (2a, 3a, 3b, 5c) and also repulsive configuration 8b which will be discussed further. Other configurations have energies in range 0.86 - 1.04 eV showing small repulsion effect. And only one configuration (14b) is clearly attractive with 0.76 eV energy. The results on OS $E_{\mathrm{C-C}}$ energies would be most efficient from the discussion of migration paths.

As it was shown in the section IIC, the migration energy of dissociation (E_{m1}) is the difference between the energy of OS-configuration and OO-configuration of initial state and the migration energy of association (E_{m2}) is the difference between the energy of OS-configuration and OO-configuration of final state. Thus, the migration energies (E_{m1} and E_{m2}) depend on the relative stability of corresponding OO- and OS-configurations.

The static carbon atom (which is located in z-site) influences the energy path of the migrating carbon atom via the initial OO-site, the transition OS-site and the final OO-site together. Since these three atomic positions occupy three

TABLE II: DFT results for octahedral–saddle carbon–carbon configurations (OS-configurations): configuration label, number of equivalent configurations (# config.), interaction energy $E_{\mathrm{C-C}}$ (in eV), migration path, dissociative and associative migration energies E_{m1} and E_{m2}, vector components $[u\,v\,w]$ and bond length $d_{\mathrm{C-C}}$ (in a_0 units).

Configuration	# config.	$E_{\mathrm{C-C}}$	Migration path	E_{m1}	E_{m2}	Vectors	$d_{\mathrm{C-C}}$
1a	4	–	–	–	–	[(±0.5 0) 0]	$\sqrt{1}/4$
2a	8	2.12	1A→ 2a → 2A	0.27	1.30	[(±1 0) ±0.5]	$\sqrt{5}/4$
3a	4	2.09	1A → 3a → 4A	0.17	2.12	[(±1.5 0) 0]	$\sqrt{9}/4$
3b	16	1.38	2A → 3b → 3A	0.55	1.12	[(±0.5 ±1) ±1]	$\sqrt{9}/4$
4a	8	1.03	2A→ 4a → 5B	0.23	1.02	[(±1 0) ±1.5]	$\sqrt{13}/4$
5a	8	0.81	4A → 5a → 5A	0.79	0.76	[(±0.5 ±2) 0]	$\sqrt{17}/4$
5b	16	0.88	3A → 5b → 6A	0.62	0.80	[(±1.5 ±1) ±1]	$\sqrt{17}/4$
5c	8	2.14	4B → 5c → 5B	0.14	2.10	[(±0.5 0) ±2]	$\sqrt{17}/4$
6a	16	0.90	5A → 6a → 6A	0.86	0.83	[(±2 ±1) ±0.5]	$\sqrt{21}/4$
7a	4	0.81	4A → 7a → 8A	0.81	0.75	[(±2.5 0) 0]	$\sqrt{25}/4$
7b	8	0.96	5A → 7b → 7A	0.80	0.80	[(±1.5 ±2) 0]	$\sqrt{25}/4$
7c	8	0.84	5B → 7c → 7B	0.90	0.83	[(±1.5 0) ±2]	$\sqrt{25}/4$
8a	16	1.00	6A → 8a → 8B	0.93	0.83	[(±2 ±1) ±1.5]	$\sqrt{29}/4$
8b	8	1.37	5B → 8b → 9B	1.33	1.30	[(±1 0) ±2.5]	$\sqrt{29}/4$
9a	16	0.92	6A → 9a → 10A	0.85	0.90	[(±2.5 ±1) ±1]	$\sqrt{33}/4$
9b	16	1.04	7B → 9b → 8B	0.89	0.88	[(±0.5 ±2) ±2]	$\sqrt{33}/4$
10a	8	0.95	8A → 10a → 9A	0.89	0.88	[(±3 0) ±0.5]	$\sqrt{37}/4$
11a	8	0.89	7A → 11a → 12A	0.86	0.90	[(±2.5 ±2) 0]	$\sqrt{41}/4$
11b	16	0.91	9A → 11b → 10A	0.84	0.89	[(±0.5 ±3) ±1]	$\sqrt{41}/4$
11c	8	0.94	7B → 11c → 12B	0.77	0.93	[(±2.5 0) ±2]	$\sqrt{41}/4$
11d	16	0.99	8B → 11d → 11A	0.81	0.95	[(±1.5 ±2) ±2]	$\sqrt{41}/4$
11e	16	1.09	9B → 11e → 10B	1.02	0.78	[(±0.5 ±1) ±3]	$\sqrt{41}/4$
12a	8	0.87	9A → 12a → 12B	0.81	0.88	[(±3 0) ±1.5]	$\sqrt{45}/4$
12b	16	0.95	8B → 12b → 13B	0.78	0.94	[(±2 ±1) ±2.5]	$\sqrt{45}/4$
13a	4	0.90	8A → 13a → 14A	0.83	0.91	[(±3.5 0) 0]	$\sqrt{49}/4$
13b	16	0.87	10A → 13b → 13A	0.85	0.86	[(±1.5 ±3) ±1]	$\sqrt{49}/4$
13c	16	1.03	10B → 13c → 13B	0.73	1.03	[(±1.5 ±1) ±3]	$\sqrt{49}/4$
14a	16	0.86	12A → 14a → 13A	0.86	0.85	[(±3 ±2) ±0.5]	$\sqrt{53}/4$
14b	8	0.76	9B → 14b → 15C	0.69	0.79	[(±1 0) ±3.5]	$\sqrt{53}/4$

different sublattices, the effect is contrasted. As mentioned before, a C atom in O-site creates a prolate distortion

whereas in S-site it creates an oblate distortion. The prolate and oblate distortions may compensate each other when they act in the same direction. In this case, the OS-configuration is "stabilized" and the interaction energy is smaller than 0.87 eV. Conversely, if the oblate and prolate distortions act in opposite directions, the OS-configuration is destabilized and the C–C interaction energy is larger than 0.87 eV.

D. Analysis of migration paths

We present our results of the migration path in the dissociation way, i.e. the C–C distance is closer in the initial state than in the final state. During an elementary migration path, the initial and final states are always OO-configurations, even if a given OO-configuration is by itself very repulsive (such as configurations 1A or 4B). All elementary migration paths were arranged by axes. Figures 8 and 9 present 4 migrations paths along z axis (we recall that the migrating atom initially sits on a z-site). Figure 10 presents 7 migration paths in the $x-y$ plane. These 11 paths cover all possible migration scenarios within a $2a_0$ radius around the static carbon atom.

It is to be noted that the transition-state OS-configuration is in most cases located at the mid transition path, i.e. at a crystallographic T-site. However, for the most repulsive configurations (2a, 3a, 4a and 5c) the saddle point is shifted towards the initial state. The migration paths $1A \to 2a \to 2A$ (Figure 8), $1A \to 3a \to 4A$ and $4B \to 5c \to 5B$ (Figure 10) have their maximum at 1/4 migration path, i.e. in the middle between initial OO-configuration and OT-configuration. For the migration path $2A \to 4a \to 5B$ the maximum is at 1/3 migration path. All 4 migration energies are very small: 0.14–0.27 eV which is related first of all to a large repulsion of two carbon atoms in the initial OO-configuration, and second, to the displacement of Fe atoms around which perturbs the topology of O- and S-sites in corresponding OO- and OS-configurations. Note that even very repulsive OO-configurations such as 1A, 2A, 3A have an activation barrier towards dissociation. In details, the migration paths will be discussed in the next subsection.

We might expect that during a migration path, when the migrating C atom is moving away from the static carbon atom along a linear path $\mathrm{O}-\mathrm{S}-\mathrm{O}-\mathrm{S}-\mathrm{O}$, the OO-configuration energy should gradually decrease down to 0 eV as the C–C repulsion decreases. For its part, the OS-configuration energy should gradually decrease down to 0.87 eV. Our results reveal a more complex behaviour.

Let's analyse the migration in $[1\,0\,k]$ direction (Figure 8b). If we look at the evolution of OO-configuration energy along the migration path, we have the expected picture: the energy decreases gradually as $1.96 \to 0.83 \to 0.04 \to 0.07 \to -0.04$ eV. However, during this path the energy of OT-configurations doesn't decrease, but it oscillates: $1.60 \to 1.06 \to 1.33 \to 0.76$ eV. In this case we need to discuss the OT-configurations to have the moving atom topologically in the T site to discuss energy trend variation. For the last two migrations in $[1\,0\,k]$ direction the OT-configuration coincides with OS-configuration, but for the first two configurations they are different because of high repulsion between the

carbon atoms. This particular difference between OS and OT-sites exists only for 2a, 3a, 4a and 5c configurations.

In the initial stage, this energy (1.60 eV) is almost twice larger than 0.87 eV, due to the large C–C repulsion. The energy of the second OS-configuration is 1.06 eV (i.e. the energy is decreased 1.5 times), but for the 3rd OS-configuration the energy increases up to 1.33 eV. It finally reaches the value of 0.76 eV, smaller than the expected final value (0.87 eV).

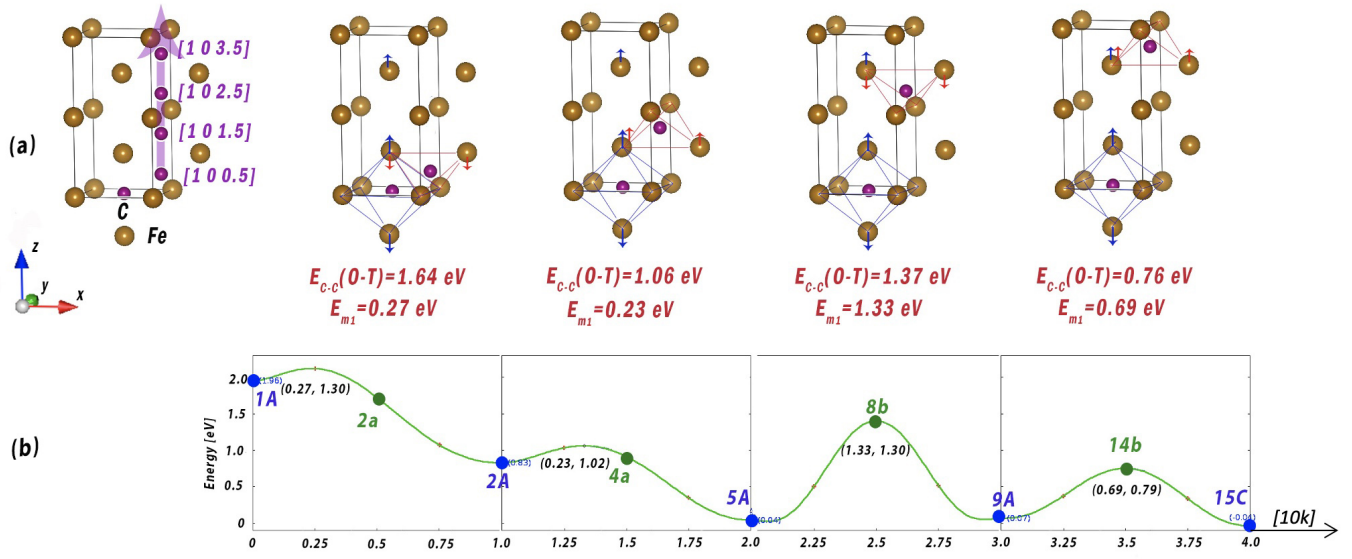

FIG. 8: Prolate-oblate interaction and its influence on the C–C interaction energy of OS-configurations. Complete migration path along $[1\,0\,k]$ vector with indication of OO- and OS-configurations along the path (b). The couple of migration energies $(E_{\mathrm{m1}}, E_{\mathrm{m2}})$ are indicated under the saddle points. Top: the atomic configurations corresponding to the tetragonal positions $k = 0.5$, 1.5, 2.5 and 3.5 (a). Blue arrows corresponds to Fe atom displacement by static C atom and red arrows - to displacement by dynamic C atom.

This oscillation can be explained by "prolate-oblate" effect, see Figure 8a. In fact, during the $9B \rightarrow 14b \rightarrow 15C$ migration path, the static and migration carbon atoms create forces acting in the same direction in nearby iron atoms, diminishing the migration energies. The opposite occurs for the $5B \rightarrow 8b \rightarrow 9B$ migration path. If we analyse other parallel axes $[1\,2\,k]$, $[3\,0\,k]$ and $[3\,2\,k]$, we observe that this effect is not present and the activation migration energy remains close to 0.87 eV.

Let's analyse carbon migration in the $x - y$ plane. The energy path along axes $[k\,0\,0]$, $[k\,1\,1]$, $[k\,2\,2]$, $[k\,0\,2]$, $[k\,2\,0]$, $[k\,3\,1]$ and $[k\,1\,3]$ are presented in Figure 10. When the migrating C atom is moving away along the $[k\,0\,0]$ direction, the C–C energy at position [1.5 0 0] is high due to the strong C–C repulsion. This insures a small migration energy E_{m1} for dissociation. Then for the next OS-configurations the C–C energy converges to the value of isolated carbon atoms ($E_{\mathrm{m}} = 0.87 \pm 0.1$ eV). Along $[k\,1\,1]$ axis we observe two small migration energies 0.55 eV and 0.62 eV corresponding to high OO-configuration energies.

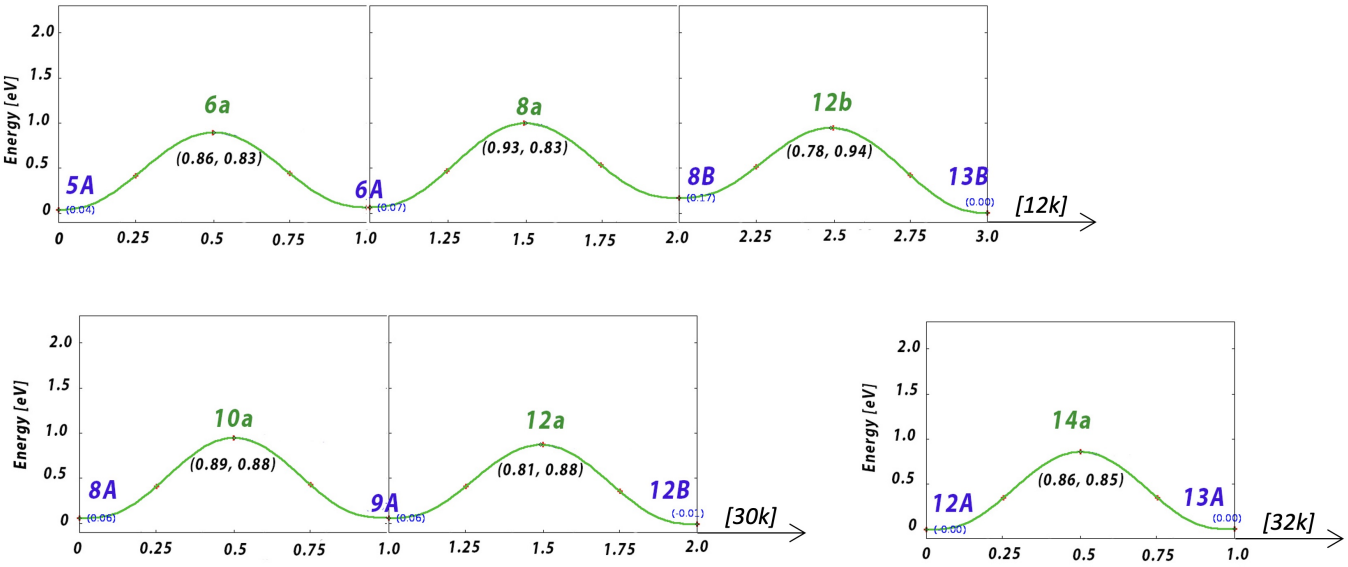

FIG. 9: Three migration paths parallel to the z-axis: $[1\,2\,k]$, $[3\,0\,k]$ and $[3\,2\,k]$.

For $[k\,2\,2]$ axis we see that the energies of configurations 7B, 9b, 8B and 11d are shifted by +0.15 eV with respect to isolated systems, thus the migration energy remains close to 0.87 eV. Only the association of 11A to 8B has larger activation energy (0.95 eV) as the configuration 11A is completely isolated. For $[k\,2\,0]$ which is more close to the static carbon atom than the previous axis $[k\,2\,2]$. We observe for the first migration smaller migration energies 0.79/0.76 eV for dissociation/association and the next two migrations have the behaviour of isolated C atom. The smaller migration energies for the first migration corresponds to the fact that OS-configuration 5a is more stable than isolated S- with O-configurations as synchronized "prolate-oblate" effect is present. Along axis $[k\,0\,2]$ we observe that 4B is very repulsive but then stabilization the system is similar to isolated. Migration along the remaining axes $[k\,3\,1]$ and $[k\,1\,3]$ proceeds as if C atoms were isolated except for the repulsive 10B configuration, which produces slight decrease in migration energies 0.73/0.78 eV for dissociation of 10B to 13B and association 10B to 9B.

E. Order parameter at equilibrium

The KMC simulation results of the Zener order parameter at different carbon contents are plotted in Fig. 11. Note that if the C-C pair interactions are neglected, the order parameter can be given by the mean-field elastic model presented in [12]. The good agreement between the analytical results and the KMC simulation results neglecting the C-C pair interactions validates the KMC approach. The mean-field approach predicts an order/disorder transition at $c = 1.27\,\text{at}\%$ and $T = 300\,\text{K}$. This transition carbon content is slightly modified due to the introduction of C-C pair interactions. According to the KMC simulations, the transition content should be between 1.27 at% and 1.30 at% at 300 K.

We investigated as well the carbon order parameter at different temperatures (cf. Fig. 12). We set the total fraction of carbon atoms to 2.50 at%. Here again, KMC simulation results neglecting the C-C pair interactions correspond well to the analytical results from the mean-field approach. Following the KMC simulation results, the order/disorder transition temperature is affected by the C-C pair interactions: the predicted transition temperature is about 590 K if the interactions between carbon atoms are neglected and about 570 K if not.

F. Tracer diffusion in ferrite and martensite

We present in Fig. 13 the KMC simulation results of the carbon tracer diffusion coefficients and the correlation factors at different carbon contents. Here again, if the C-C pair interactions are neglected, the diffusion coefficients can be given by an analytical approach presented in [12]. We have a good agreement between the analytical results and the KMC simulation results neglecting the C-C pair interactions. As predicted in previous studies [12], carbon diffusion is highly anisotropic due to carbon ordering. The carbon diffusivity along the z-axis (i.e., the Zener ordering direction) is much lower than that along x and y directions (perpendicular to the ordering direction). Comparison between the KMC simulation results with and without considering the C-C pair interactions highlights the effect of these interactions on the kinetic properties. The carbon diffusivity along the z-axis is significantly increased by the C-C repulsive interactions (up to 10 times at high carbon contents). The increase in carbon diffusivity along x and y directions are less important (e.g., about 20% when $c = 4.0$ at% at 300 K). Moreover, the interactions between carbon atoms lead to important kinetic correlations: the correlation factors are smaller than 0.2 when $c > 3.0$ at% at 300 K.

Also, we studied the effect of C-C pair interactions on the kinetic properties at different temperatures (cf. Fig. 14). According to the simulation results, the increase of the carbon diffusivity is significant at low temperatures. For example, the acceleration of the carbon diffusivity along the z direction is over 10 times at $T < 300$ K. A relevant kinetic correlation occurs at low temperatures: the correlation factors are smaller than 0.4 at $T < 400$ K.

As presented in Table II, most of the migration barriers between the investigated configurations are smaller than the isolated carbon migration barrier (0.87 eV). This decrease of migration barriers explains the increase of the carbon diffusivity. We consider the migration paths along z-direction (cf. Fig. 9 and Fig. 10). As mentioned in Section III D, the carbon migration path along [1 2 k], [3 0 k] and [3 2 k] is similar to the isolated one because the activation energy is close to 0.87 eV. However, a "prolate-oblate" effect occurs along the [1 0 k]-migration path. The carbon atom can be "trapped" in 5A configuration by performing forward and backward jumps connecting to 2A configurations. This effect should be responsible for the important kinetic correlation along the z-direction. As for the migration paths in the x-y plane, there is no important oscillation of the migration barriers as seen along the z-direction. Hence, it is unlikely for the carbon atoms to be trapped in the x-y plane. However, the migration paths along [k 0 0], [k 1 1] and [k 0 2] are particularly different from the isolated one (i.e., the random diffusion path) due to the important C–C

repulsive interactions in 1A, 2A and 4B OO-configurations—very small carbon migration barriers for an "avoid" from these configurations (0.17 eV, 0.55 eV and 0.89 eV, respectively). This difference leads to the kinetic correlations along x- and y-directions because the carbon atoms tend to "escape" each other.

The tracer diffusion coefficients of carbon atoms in Fe-C martensite were previously calculated by Lawrence et al. [26] by applying the molecular dynamic (MD) simulation based on an EAM potential. This simulation was limited to high temperature (> 800 K) so that the statistic to measure the MSD was sufficient in the time scale of MD. As predicted in their studies, our results also showed slow carbon diffusion in martensite. However, we cannot quantitatively compare the diffusion coefficients presented in the present study with those obtained in [26] because, on one hand, the investigated carbon concentrations and temperatures are not the same; and on the other hand, our simulation is based on a more recent energy database of the elastic dipoles and the migration barriers given by the DFT calculation. Therefore, the diffusion properties obtained in this paper must be different from those of Lawrence et al. [26]. Compared with their studies, our approach based on KMC simulation allows to compute the tracer diffusion coefficient at a wider range of temperature (> 200 K in the present study). Moreover, we provide a more complete investigation into the anisotropy of the carbon diffusion, as well as the kinetic correlations in martensite.

IV. CONCLUSION

We studied by a DFT method short range C–C interactions in ferrite and their influence on the migration energies of carbon. Stable octa-octa (OO) and unstable octa-saddle state (OS) configurations were investigated.

We found that the configuration stability is not always a simple function of C–C distance and there is no direct correlation in energy between neighbours OO- and OS-configurations. The absence of correlation is related to the fact that during a simple migration path the migrating C atom goes through 3 sublattices (x, y, z) while a static carbon atom remains always in the same sublattice. Concerning OO-configurations, in most cases the interaction energy is close to 0.0 eV. However, when 2 carbon atoms occupy the same sublattice the interaction energy rises to 0.10–0.30 eV. In the case of small C–C distances the interaction energy increases up to 2.0 eV, indicating strong repulsion.

For the first time the OS-configurations were studied in detail by the NEB technique. These configurations are unstable, being in the vicinity of tetrahedral sites. For OS-configurations we observed an interesting effect of "oblate-prolate" interactions: when two carbon atoms are located in the same sublattice some configurations reduce the interaction energy (0.60–0.80 eV) while others increase it, compared to an isolated carbon atom (0.95–1.10 eV).

Finally the migration energy was studied for all configurations where C–C distance is in the limit of $2a_0$. We observed a range of small migration energies (0.14–0.27 eV) and a larger range of medium migration energies (0.60–0.80 eV). Most configurations have migration energies (0.87±0.05 eV) close to the isolated system. Some configurations have migration energies larger than 0.92 eV.

Thus, this work showed that the role of static carbon atom is not negligible for the diffusion phenomena and migration energy varies from 0.15 eV up to 2.12 eV while for the single C atom migration the energy is 0.87 eV. The computed energy database was used to calculate the carbon order parameter and diffusion coefficients by kinetic Monte Carlo simulations. According to our simulations, C–C pair repulsive interactions lead to (1) the modification of the order/disorder transition conditions depending on the carbon content and temperature; (2) the increase of the carbon diffusivity, especially along the Zener ordering direction (up to ten times); (3) the important kinetic correlations. These results clearly show that while calculated by mean-field model diffusion coefficient D_x is not highly depend on C-C interactions (at 4 % atomic content of C, D_x is about 10% higher when C-C interactions are included), the diffusion coefficient D_z is highly depended of C-C interactions and the diffusion coefficient D_z is one order of magnitude higher (at 4 % atomic content of C) when the C-C interactions are taken into account. These effects should be taken into account for an accurate prediction of low-temperature ageing in ferritic and martensitic Fe-C alloys.

CRediT authorship contribution statement

Dmytro Kandaskalov: Conceptualization, Methodology, Writing – original draft, Writing – article editing.

Liangzhao Huang: Methodology, Writing - article, Conceptualization

Johnathan Emo: Methodology.

Philippe Maugis: Supervision, Conceptualization and Writing - editing

Acknowledgments

The Agence Nationale de la Recherche (contract C-TRAM ANR-18-CE92-0021) is thanked for its financial support. Centre de Calcul Intensif d'Aix-Marseille is acknowledged for granting access to its high performance computing resources. This work was also supported by the HPC resources of IDRIS under allocation number 100524 made by GENCI.

Bibliography

[1] H. Mehrer, Diffusion in Solids, Springer, 2007.

[2] P. Heitjans, J. Karger, Eds. (2005). Diffusion in condensed matter: Methods, Materials, Models (2nd ed.).

[3] R.P. Smith, The diffusivity of carbon in iron by the steadystate method, Acta Metal. 1 (1953) 578-587. https://doi.org/10.1016/0001-6160(53)90088-1

[4] C Garcia-Mateo, JA Jiménez, HW Yen, MK Miller, L Morales-Rivas et al., Low temperature bainitic ferrite: Evidence of carbon super-saturation and tetragonality, Acta Materialia 91 (2015) 162-173. https://doi.org/10.1016/j.actamat.2015.03.018

[5] J. Wilde, A. Cerezo, G.D.W. Smith, Three-dimensional atomic-scale mapping of a Cottrell atmosphere around a dislocation in iron, Scripta Mater. 43 (2000) 39-48. https://doi.org/10.1016/S1359-6462(00)00361-4

[6] C. Zhu, A. Cerezo, G.D.W. Smith, Carbide Characterisation in Low Temperature Tempered Steels, Ultramicroscopy 109 (2009) 545-552. https://doi.org/10.1016/j.ultramic.2008.12.007

[7] P. Haasen, The early stages of the decomposition of alloys, Metall. Trans. A 16A (1985) 1173-1184. https://doi.org/10.1007/BF02643997

[8] P. Rochegude, J. Foct, Interstitial Atom Ordering in Binary Fe-N Solid Solutions Studied by Mössbauer Spectrometry, Phys. Status Solidi A 98 (1986) 51-62. https://doi.org/10.1002/pssa.2210980106

[9] P. Maugis, F. Danoix, M. Dumont, S. Curelea, S. Cazottes, H. Zapolsky et al., Mater. Lett. 214 (2018) 213-216. https://doi.org/10.1016/j.jallcom.2018.08.060.

[10] K.A. Taylor, L. Chang, G.B. Olson, G.D.W. Smith, M. Cohen, J.B. Vander Sande, Spinodal decomposition during aging of Fe-Ni-C martensites, Metall. Trans. A. 20 (1989) 2717-2737. https://doi.org/10.1007/BF02670166

[11] A. Rajesh and J. Venkatesh, Evaluation and Diffusion Assessment for Surface Hardening Processes, J. Material Sci. Eng. 3 (2014) 146. https://doi.org/10.4172/2169-0022.100014

[12] P. Maugis, S. Chentouf, D. Connétable, Stress-controlled carbon diffusion channeling in bct-iron: A mean-field theory, J. Alloys Compd. 769 (2018) 1121-1131. https://doi.org/10.1016/j.jallcom.2018.08.060

[13] J. Svoboda, G.A. Zickler, F.D. Fischer, An innovative concept for interstitial diffusion in stressed crystals, Int. J. Solid Structure 134 (2018) 173-180. https://doi.org/10.1016/j.ijsolstr.2017.10.036

[14] R. Bagramov, D. Mari and W. Benoit, Internal friction in a martensitic high-carbon steel, Phil. Mag. A 81 (2001) 2797-2808. https://doi.org/10.1080/01418610108217165

[15] M.P Staiger, A Brownrigg, P.D Hodgson and C.H.J Davies, Materials Science and Engineering A 364 (2004) 35-47.

[16] J.B. Rellick and C.J. McMahon, Intergranular embrittlement of iron-carbon alloys by impurities, Metallurgical Transactions 5 (1974) 2439-2450. https://doi.org/10.1007/BF02644027

[17] G.M. Green, R. Taggart, D.H. Polonis, Influence of microstructure on the erosion of plain carbon steels, Metallography 14 (1981) 191-212.

[18] C.A. Wert, Diffusion Coefficient of C in -Iron, Phys. Rev. 79 (1950) 601-605. https://doi.org/10.1103/PhysRev.79.601

[19] Y. Iijima, J. Alloys Compd. 234 (1996) 290-294. https://doi.org/10.1016/0925-8388(95)02104-3

[20] J.L. Snoek, Physica Amsterdam **8**, 711 (1941).

[21] D. N. Beshers, Diffusion in Body-Centered Cubic Metals American Society for Metals, Metals Park, OH, (1965), p. 149.

[22] R.H. Condit and D.N. Beshers, Interstitial Diffusion in the B.C.C. Lattice, Trans. Metall. Soc. AIME 239 (1967) 680-683.

[23] R.B. McLellan, M.L. Rudee, and T. Ishibachi, The thermodynamics of dilute interstitial solid solutions with dual-site occupancy and its application to the diffusion of carbon in alpha iron,Trans. Metall. Soc. AIME 233 (1965) 1938-1943 .

[24] J.R.G. da Silva, R.B. McLellan, Diffusion of carbon and nitrogen in BCC iron, Mater. Sci. Eng. 26 (1976) 83–87.

[25] N. DeCristofaro, R. Kaplow, W.S. Owen, The kinetics of carbon clustering in martensite, Metall. Trans. A. 9 (1978) 821-825. https://doi.org/10.1007/BF02649791

[26] B. Lawrence, C.W. Sinclair, M. Perez, Carbon diffusion in supersaturated ferrite: a comparison of mean-field and atomistic predictions, Model. Simul. Mater. Sci. Eng. 22 (2014) 1-17 . https://doi.org/10.1088/0965-0393/22/6/065003

[27] D.E. Jiang and E. A. Carter, Carbon dissolution and diffusion in ferrite and austenite from first principles, Phys. Rev. B 67 (2003) 214103-214113. https://doi.org/10.1103/PhysRevB.67.214103

[28] P. Maugis, D. Kandaskalov, Revisiting the pressure effect on carbon migration in iron, Mater. Lett. 270 (2020) 127725-127728. https://doi.org/10.1016/j.matlet.2020.127725

[29] C.S. Becquart, J.M. Raulot, G. Bencteux, C. Domain, M. Perez, S. Garruchet et al., Atomistic modeling of an Fe system with a small concentration of C, Comput. Mater. Sci. 40 (2007) 119-129. https://doi:10.1016/j.commatsci.2006.11.005

[30] S. Chentouf, S. Cazottes, F. Danoix, M. Gouné, H. Zapolsky, P. Maugis, Effect of interstitial carbon distribution and nickel substitution on the tetragonality of martensite: A first-principles study, Intermetallics 89 (2017) 92-99. https://doi.org/10.1016/j.intermet.2017.05.022

[31] A. V. Ruban, Self-trapping of carbon atoms in ′-Fe during the martensitic transformation: A qualitative picture from ab initio calculations, Phys. Rev. B 90 (2014) 144106. https://doi.org/10.1103/PhysRevB.90.144106

[32] C. Domain, C. S. Becquart, and J. Foct, Ab initio study of foreign interstitial atom (C, N) interactions with intrinsic point defects in -Fe, Phys. Rev. B 69 (2004), 144112-144116. https://doi.org/10.1103/PhysRevB.69.144112

[33] G. Kresse and J. Hafner, Ab initio molecular dynamics for liquid metals, Phys. Rev. B 47 (1993) 558. https://doi.org/10.1103/PhysRevB.47.558 ; G. Kresse and J. Hafner, Ab initio molecular-dynamics simulation of the liquid-metal–amorphous-semiconductor transition in germanium, Phys. Rev. B 49 (1994) 14251. https://doi.org/10.1103/PhysRevB.49.14251; G. Kresse, and J. Furthmuller, Efficient iterative schemes for ab initio total-energy calculations using a plane-wave basis set, Phys. Rev. B 54 (1996) 11169 . https://doi.org/10.1103/PhysRevB.54.11169; G. Kresse, and J. Furthmuller, Efficiency of ab-initio total energy calculations for metals and semiconductors using a plane-wave basis set, Comput. Mater. Sci. 6 (1996) 15. https://doi.org/10.1016/0927-0256(96)00008-0

[34] G. Kresse and D. Joubert, From ultrasoft pseudopotentials to the projector augmented-wave method, Phys. Rev. B 59 (1999) 1758. https://doi.org/10.1103/PhysRevB.59.1758

[35] J. P. Perdew, K. Burke and M. Ernzerhof, Generalized Gradient Approximation Made Simple, Phys. Rev. Lett., 77 (1996) 3865. https://doi.org/10.1103/PhysRevLett.77.3865

[36] H.J. Monkhorst and J.D. Pack, Special points for Brillouin-zone integrations, Phys. Rev. B 13 (1976) 5188. https://doi.org/10.1103/PhysRevB.13.5188

[37] C. M. Fang, M. A. van Huis, B. J. Thijsse, and H. W. Zandbergen, Stability and crystal structures of iron carbides: A comparison between the semi-empirical modified embedded atom method and quantum-mechanical DFT calculations, Phys. Rev. B 85 (2012) 054116. https://doi.org/10.1103/PhysRevB.85.054116

[38] D. Connetable and P. Maugis, First principle calculations of the -Fe3AlC perovskite and iron–aluminium intermetallics, Intermetallics, 16 (2008) 345-352. https://doi.org/10.1016/j.intermet.2007.09.011

[39] D. Kandaskalov, C. Mijoule and D. Connétable, Study of multivacancies in alpha Fe, Journal of Nuclear Materials 441 (2013) 168-177. http://dx.doi.org/10.1016/j.jnucmat.2013.05.030

[40] D. Kandaskalov and P. Maugis A first-principle study of the structural, elastic, lattice dynamical and thermodynamic properties of a"-Fe16C2 and a"-Fe16N2 phases, Computational Materials Science 128 (2017) 278-286. http://dx.doi.org/10.1016/j.commatsci.2016.11.022

[41] C. Kittel, Introduction to Solid State Physics, 6th ed. Wiley, New York, 1986.

[42] Henkelman, J.; Jonsson, H. J., Nudged-elastic band method with two climbing images: Finding transition states in complex energy landscapes, Chem. Phys. 113 (2000) 9978-9985. https://doi.org/10.1063/1.4905209

[43] Henkelman, J.; Uberuaga, B. P.; Jonsson H. J., A climbing image nudged elastic band method for finding saddle points and minimum energy paths, Chem. Phys. 113 (2000) 9901-9904. https://doi.org/10.1063/1.1329672

[44] S. Garruchet, M. Perez, Modelling the carbon Snoek peak in ferrite: Coupling moleculardynamics and kinetic Monte-Carlo simulations, Comput. Mater. Sci. 43 (2008) 286-292. https://doi:10.1016/j.commatsci.2007.11.004

[45] D.H.R. Fors, G. Wahnström, Nature of boron solution and diffusion in -iron, Phys. Rev. B 77 (2008) 132102. https://doi.org/10.1103/PhysRevB.77.132102

[46] M. Souissi, Y. Chen, M.H.F. Sluiter, H. Numakura, Ab initio characterization of B, C, N, and O in bec iron: solution and migration energies and elastic strain fields, Comput. Mater. Sei. 124 (2016) 249-258. https://doi.org/10.1016/j.commatsci.2016.07.037.

[47] A.F. Bialon, T. Hammerschmidt, R. Drautz, Ab initio study of boron in -iron: Migration barriers and interaction with point defects, Phys. Rev. B 87 (2013) 104109 https://doi.org/10.1103/PhysRevB.87.104109

[48] D. Kandaskalov, P. Maugis, Thermodynamic stabilities in the Fe - Fe 16C2 system: Influence of carbon-carbon interactions studied by DFT, Comput. Mater. Sci. 150 (2018) 524-534. https://doi.org/10.1016/j.commatsci.2018.04.025

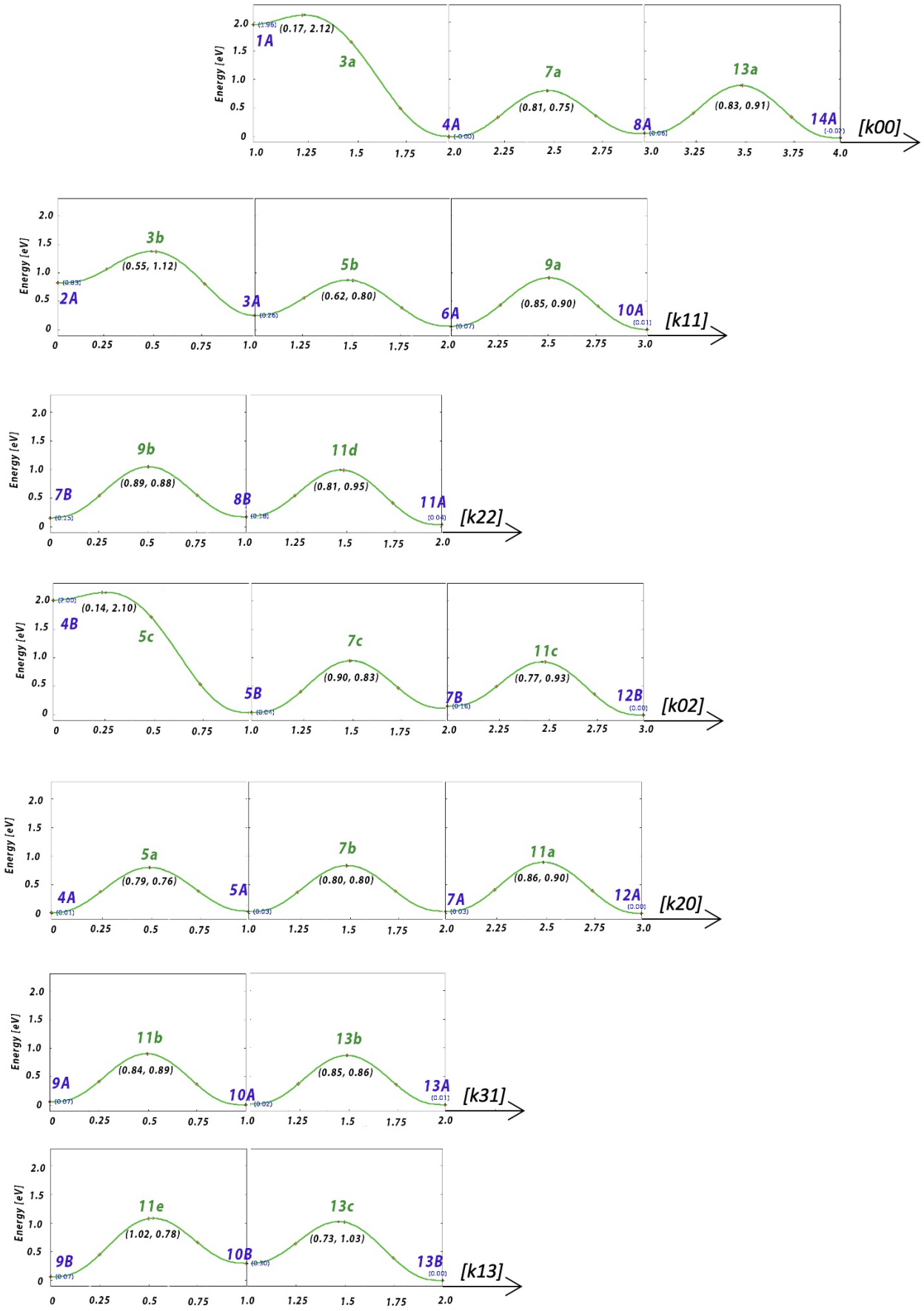

FIG. 10: All 7 migration paths for C atom developing along x axis: $[k\,0\,0]$, $[k\,1\,1]$, $[k\,2\,2]$, $[k\,2\,0]$, $[k\,0\,2]$, $[k\,1\,3]$ and $[k\,3\,1]$.

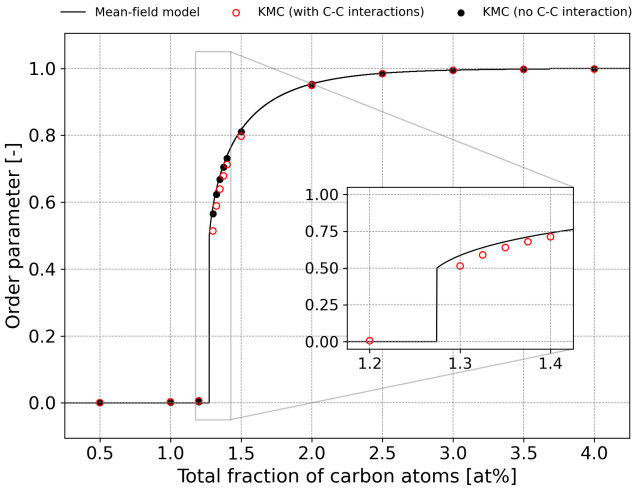

FIG. 11: Order parameter as a function of the carbon contents at 300 K. The filled and unfilled points are the KMC simulation results. The solid lines are computed using the mean-field elastic model presented in [12], in which the C-C interactions are not considered. The inset is the zoom of the simulation results around the order/disorder transition carbon content.

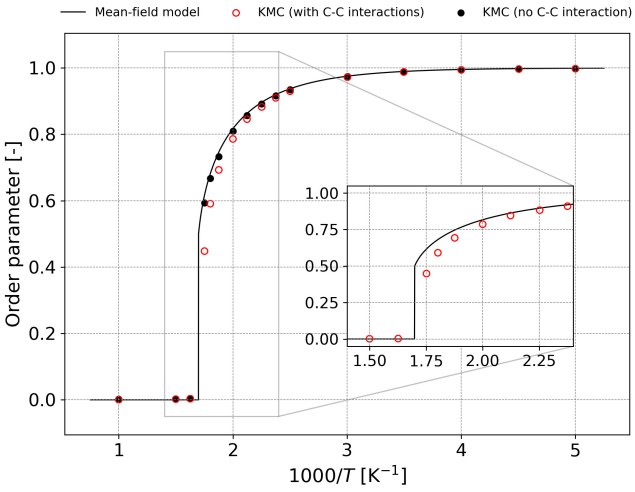

FIG. 12: Order parameter as a function of temperature. The filled and unfilled points are the KMC simulation results. The solid lines are computed using the mean-field elastic model presented in [12], in which the C-C interactions are not considered. The total fraction of carbon is set to 2.5 at% in the simulation. The inset is the zoom of the simulation results around the order/disorder transition temperature.

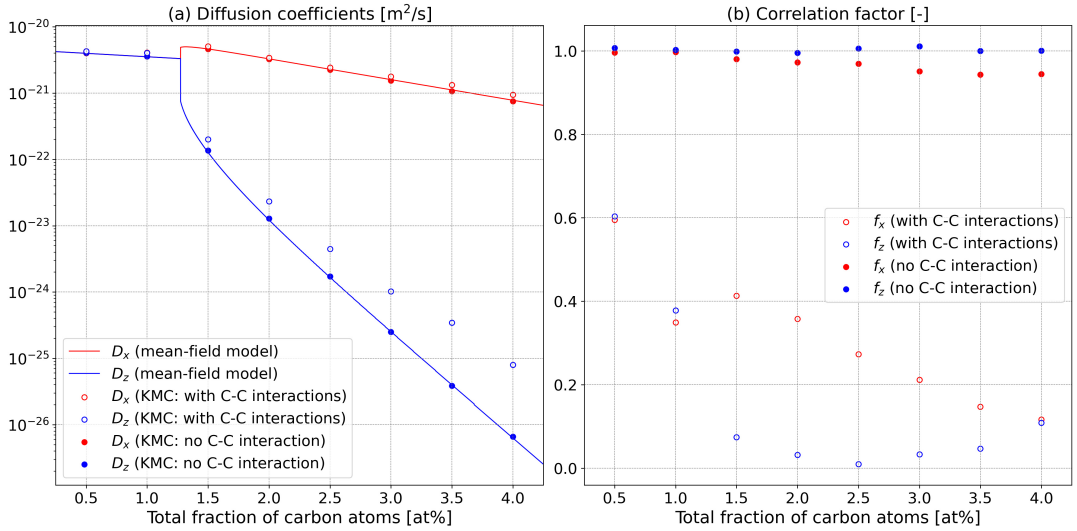

FIG. 13: Tracer diffusion coefficients and correlation factors as a function of the carbon contents at 300 K. The filled and unfilled points are the KMC simulation results. The solid lines are computed using the mean-field elastic model presented in [12], in which the C-C interactions are not considered.

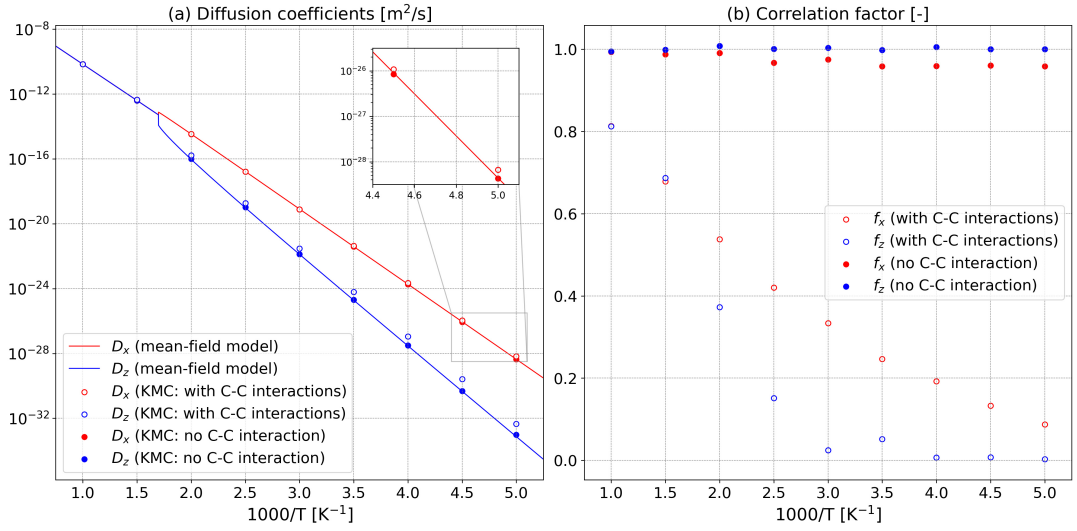

FIG. 14: Tracer diffusion coefficients and correlation factors as a function of temperature with the total fraction of carbon $c = 2.5\,\text{at}\%$. The filled and unfilled points are the KMC simulation results. The solid lines are computed using the mean-field elastic model presented in [12], in which the C-C interactions are not considered.